ORNL/TM-2022/2805

# Electromagnetic Field Simulation Utilizing VERTEX


C. Plechaty
R. Glasby
S. Slattery
F. Curtis
I. Bodey

**May 2023**

OAK RIDGE National Laboratory

ORNL IS MANAGED BY UT-BATTELLE LLC FOR THE US DEPARTMENT OF ENERGY

**ORNL/TM-2022/2805**

Enrichment Science and Engineering Division

# Electromagnetic Field Simulation Utilizing VERTEX

C. Plechaty, R. Glasby, S. Slattery, F. Curtis, and I. Bodey

March 2023

Prepared by
OAK RIDGE NATIONAL LABORATORY
Oak Ridge, TN 37831
managed by
UT-Battelle LLC
for the
US DEPARTMENT OF ENERGY
under contract DE-AC05-00OR22725

# CONTENTS

## LIST OF FIGURES

## LIST OF TABLES

# 1. INTRODUCTION

The understanding of electromagnetic fields is essential for many core applications at Oak Ridge National Laboratory (ORNL). Electromagnetic fields play an important role in particle accelerators, antennas, electric motors, power grids, and are a principal part of nuclear fusion. The team is developeing a numerical solver called VERTEX-MAXWELL to solve Maxwell's equation, allowing for the complex behavior of electromagnetic fields to be modeled utilizing VERTEX's framework [2]. The VERTEX framework provides tools required to solve complex multiphysics problems in an environment optimized for high performance computing. The current framework includes an implicit hyperbolic solver, unstructured adaptive meshes, and particle-mesh integration algorithms.

VERTEX-MAXWELL will contribute to VERTEX's overall strategy and research priorities by utilizing VERTEX-CORE to implement higher-order temporal and spatial discretization methods. VERTEX-CORE allows for efficient hyperbolic partial differential equation spatial/temporal stabilization through differential eigensystem solvers and singly diagonal implicit Runge-Kutta (SDIRK) methods to advance the field in time. VERTEX-MAXWELL will solve for electromagnetic fields on arbitrary unstructured meshes whereby input/output data structures are provided by VERTEX-CORE. Implementation of volumetric terms for the fully coupled time-domain Maxwell's equations are also provided by VERTEX-CORE. The partial differential equations will be implemented with automatic differentiation [3] in the Trilinos framework developed by Sandia National Laboratory. Newton's method will be used to progress solutions implicitly in the time domain. The use of correction potentials [4] will provide corrections to the field divergences to alleviate common numerical issues with Maxwell solvers.

VERTEX-MAXWELL will incorporate three research objectives during its development. First, VERTEX-MAXWELL will provide a generalized method to solve Maxwell's equations in the time domain. The solver will ultimately be incorporated into future efforts that simulate the use of plasma in isotope separation and the development of fusion blankets, wherein the dynamics of the electromagnetic fields play an important role.

Second, the team aims to implement a variety of boundary/material interface conditions for a wide variety of electromagnetic fields. Material interfaces will be represented by numerical jumps in current, permeability, and/or permittivity. These interfaces will be simulated spatially through the discontinuous Galerkin module in VERTEX-CORE. Far-field nonreflecting boundaries will be simulated with the characteristic method that utilizes VERTEX-CORE's eigensystem solver.

Finally, the team aims to verify the numerical order of accuracy of VERTEX-MAXWELL and validate the solution methodology by comparing computed results to experimental data and problems with analytical or known solutions. The validation cases considered are discussed in section 3.

# 2. BACKGROUND

## 2.1 GOVERNING EQUATIONS

Maxwell's equations govern electromagnetic phenomena, and can be written in their differential forms as (in SI units) [5]:

$$\nabla \times \mathbf{E} = -\frac{\partial \mathbf{B}}{\partial t} \tag{1}$$

$$\nabla \times \mathbf{H} = \frac{\partial \mathbf{D}}{\partial t} + \mathbf{J} \tag{2}$$

$$\nabla \cdot \mathbf{D} = \rho_q \tag{3}$$

$$\nabla \cdot \mathbf{B} = 0 \tag{4}$$

where $\mathbf{B}$ is the magnetic field vector, $\mathbf{E}$ is the electric field vector, $\rho_q$ is the charge density, and $\mathbf{J}$ is the current density vector. For linear materials, which are considered herein, the constitutive relations for $\mathbf{D}$ and $\mathbf{H}$ are:

$$\mathbf{D} = \epsilon \mathbf{E} \tag{5}$$

$$\mathbf{B} = \mu \mathbf{H} \tag{6}$$

where $\mu$ and $\epsilon$ are the permeability and permittivity, respectively. The relationship between the relative permeability and permittivity are $\mu_r = \mu/\mu_0$ and $\epsilon_r = \epsilon/\epsilon_0$, where $\mu_0$ is the permeability of free space and $\epsilon_0$ is the permittivity of free space. For linear materials, polarization and magnetization effects are neatly accounted for by the specification of the material-dependant values for $\epsilon_r$ and $\mu_r$. This treatment is sufficient for application in describing a large variety of electromagnetic behavior.

In the Maxwell system, Equation 1 is referred to as Faraday's law and describes how varying magnetic flux density can induce an electric field, and vice versa. Equation 2 is Ampere's law and describes how a current or time-varying electric field can produce a magnetic field. The term containing $\frac{\partial \mathbf{D}}{\partial t}$ is called the displacement current or Maxwell's correction. Guass's law is provided by Equation 3 and describes the relationship between charge and the electric field. Finally, Equation 4 accounts for the lack of the observance of magnetic monopoles experimentally.

In Equations 1–6, an expression for $\rho_q$ and $\mathbf{J}$ is required to close the system of equations. Taking the divergence of Equation 2 and applying Equation 3 yields the continuity equation:

$$\frac{\partial \rho_q}{\partial t} = -\nabla \cdot \mathbf{J} \tag{7}$$

Physically, Equation 7 states that diverging current flow out of a volume element must be balanced by a time-varying charge density in the absence of source terms (e.g., ionization). Because of errors introduced by discretization, the continuity equation can be hard to satisfy numerically. Furthermore, the phenomenology governing $\rho_q$ and $\mathbf{J}$ can be complex, arising from individual behavior of all charged particle species present. In some cases, $\rho_q$ and $\mathbf{J}$ must be obtained from other computations, such as the use of Particle-in-cell or some form of the magnetohydrodynamic (MHD) equations (e.g., ideal-MHD, Hall-MHD, two-fluid MHD). In some situations, the continuity equation may not be strictly enforced. In future VERTEX efforts, more complex models for $\rho_q$ and $\mathbf{J}$ will be incorporated into the framework.

For the model developed here, the team will treat $\rho_q$ and $\mathbf{J}$ as self-consistently defined inputs either specified by the user or determined through other computational methods or theory. This design philosophy enables a very versatile way to treat electromagnetic problems in VERTEX. For example, free space conditions can be enforced by simply setting $\mathbf{J}$=0 and $\rho_q$ =0. Alternatively, by defining and specific time-varying current density distribution, the fields produced by an antenna can be simulated, enabling the design for fusion applications. This formulation also provides a means to account for the presence of conductive material via Ohms law:

$$\mathbf{J} = \sigma \mathbf{E} \tag{8}$$

To provide a stable means to solve the Maxwell system (Equations 1–6), correction potentials will be introduced to enforce the divergence constraints and provide a way to couple changes in $\rho_q$ and $\boldsymbol{\nabla} \cdot \mathbf{D}$. When the correction potentials for the electric field $\phi$ and magnetic field $\psi$ are utilized in the Maxwell system, the following are obtained [4]:

$$\frac{\partial \mathbf{B}}{\partial t} + \boldsymbol{\nabla} \times \mathbf{E} + \beta \nabla \psi = 0 \tag{9}$$

$$\frac{\partial \mathbf{E}}{\partial t} - c^2 \boldsymbol{\nabla} \times \mathbf{B} + \chi c^2 \nabla \phi = -\mathbf{J}/\epsilon \tag{10}$$

$$\frac{1}{\chi}\frac{\partial \phi}{\partial t} + \boldsymbol{\nabla} \cdot \mathbf{E} = \rho_q/\epsilon \tag{11}$$

$$\frac{1}{\beta}\frac{\partial \psi}{\partial t} + c^2 \boldsymbol{\nabla} \cdot \mathbf{B} = 0 \tag{12}$$

where $\chi$ and $\beta$ govern the strength of the correction, and $c$ is the speed of light in vacuum. For $\chi = \beta = 0$, $\phi$ and $\psi$ do not evolve in time and Equations 9–12 revert back to the original form represented by Equations 1–6.

The correction potentials $\phi$ and $\psi$ allow the system of equations to be solved, while simultaneously enforcing the divergence constraints ($\boldsymbol{\nabla} \cdot \mathbf{B}$ and $\boldsymbol{\nabla} \cdot \mathbf{E}$) to account for numerical discretion errors. The parameters $\chi$ and $\beta$ (typically of order 1) are usually fixed in time [4]. For implementation within VERTEX, we will explore the use of dynamic $\chi$ and $\beta$ values that are determined by sub cycling methods to enforce physical behavior of the solution to high accuracy.

Equations 9–12 are a set of linear differential equations that can be reorganized into hyperbolic form and solved numerically using upwinding schemes in VERTEX. In VERTEX, the set of equations are

numerically integrated by employing the unstructured higher-order accurate Streamline Upwind Petrov-Galerkin (SUPG) finite-element method for spatial discretization [6]. Since the equation set considered is unsteady, solution convergence is accelerated and numerical robustness is enhanced by utilizing implicit time stepping. The linear system incurred from implicit time stepping is solved using the Generalized Minimum Residual (GMRES) algorithm with preconditioning [7].

## 2.2 IMPLEMENTATION IN VERTEX

For numerical stability and implementation within VERTEX, the 3D Maxwell's equations with the magnetic and electric correction potentials are utilized by first casting the set of equations into dimensionless form. This is accomplished by expressing Equations 9–12 in terms of several dimensionless quantities:

$$\begin{array}{cc} \mathbf{J} = \mathbf{J}' v_o \rho_0 & \rho_q = \rho_q' \rho_0 \\ \mathbf{B} = \mathbf{B}' B_0 & \mathbf{E} = \mathbf{E}' B_0 v_0 \\ \psi = \psi' B_0 v_0 & \phi = \phi' B_0 \\ t_0 = L/v_0 & \text{x=x'L} \\ E_0 = v_0 B_0 & J_0 = v_0 \rho_0 \end{array}$$

where dimensionless quantities are denoted with a prime ($'$), and $B_0$, $t_0$, $L$, $v_0$, and $\rho_0$ denote the characteristic magnetic field, timescale, spatial scale, velocity, and charge density, respectively. The choice in these quantities forces $\nabla \rightarrow \frac{1}{L}\nabla'$, and $\frac{\partial}{\partial t} \rightarrow \frac{1}{t_0}\frac{\partial}{\partial t'}$, where derivatives are taken with respect to the dimensionless variables. By incorporating the dimensionless quantities into Equations 9–12, the following is obtained:

$$\frac{\partial \mathbf{B}'}{\partial t'} + \nabla' \times \mathbf{E}' + \beta' \nabla' \psi' = 0 \tag{13}$$

$$\frac{\partial \mathbf{E}'}{\partial t'} - c'^2 \nabla' \times \mathbf{B}' + \chi c'^2 \nabla' \phi' = -\Gamma \mathbf{J}' \tag{14}$$

$$\frac{\partial \phi'}{\partial t'} + \chi' \nabla' \cdot \mathbf{E}' = \chi' \Gamma \rho_q' \tag{15}$$

$$\frac{\partial \psi'}{\partial t'} + \beta' c'^2 \nabla' \cdot \mathbf{B}' = 0 \tag{16}$$

Equations 13–16 provide the space and time evolution of Maxwell's equations, and the correction potentials, in non-dimensional form. The parameter $\Gamma$ plays a special role in the behavior of the system, and is strictly composed of the characteristic scaling parameters defined above, and can be expressed several ways to provide physical insight:

$$\Gamma = \frac{\rho_0 L}{B_0 \epsilon_0 v_0} \tag{17}$$

$$= \frac{\rho_0 L}{E_0 \epsilon_0} \tag{18}$$

$$= \frac{J_0 t_0}{E_0 \epsilon_0} \tag{19}$$

Mathematically, the magnitude of $\Gamma$ determines the strength that $\rho'_q$ and $\mathbf{J}'$ couples into the system, thereby controlling the generation of electric and magnetic fields for the timescales ($t_0$) and spatial scales ($L$) chosen for a particular problem. Numerically, $\Gamma$ provides a measure of the strength of the source vector (discussed in Section 2.3), which may require the use of stiff time-integration methods. Its use will be demonstrated in future sections.

## 2.3 HYPERBOLIC FORM AND NUMERICAL SOLUTION

The solvers employed in VERTEX are capable of solving systems of equations in hyperbolic form. For Equations 13–16 we consider the form:

$$\frac{\partial \mathbf{U}}{\partial t} + \boldsymbol{\nabla} \cdot \mathbf{F} = \mathbf{S} \tag{20}$$

where $\mathbf{U}$ is called the parameter vector, $\mathbf{F}$ is known as the flux vector, and the source vector is $\mathbf{S}$. The flux vector can be expanded using $\mathbf{F}_x$, $\mathbf{G}_y$, and $\mathbf{H}_z$, to treat the flux in terms of derivatives in each spatial direction:

$$\frac{\partial \mathbf{U}}{\partial t} + \frac{\partial \mathbf{F}_x}{\partial x} + \frac{\partial \mathbf{G}_y}{\partial y} + \frac{\partial \mathbf{H}_z}{\partial z} = \mathbf{S} \tag{21}$$

Equations 13–16 can be cast into the form of Equation 21 with suitable choices for $\mathbf{U}$, $\mathbf{S}$, $\mathbf{F}_x$, $\mathbf{G}_y$, and $\mathbf{H}_z$:

$$\mathbf{F}_x = \begin{pmatrix} \beta'\psi' \\ -E'_z \\ E'_y \\ c'^2\chi'\phi' \\ B'_z c'^2 \\ -B'_y c'^2 \\ E'_x \\ B'_x \end{pmatrix} \qquad \mathbf{G}_y = \begin{pmatrix} E'_z \\ \beta'\psi' \\ -E'_x \\ -c'^2 B'_z \\ c'^2\chi'\phi' \\ c'^2 B'_x \\ E'_y \\ B'_y \end{pmatrix} \qquad \mathbf{H}_z = \begin{pmatrix} -E'_y \\ E'_x \\ \beta'\psi' \\ c'^2 B'_y \\ -c'^2 B'_x \\ c'^2\chi'\phi' \\ E'_z \\ B'_z \end{pmatrix}$$

$$\mathbf{U} = \begin{pmatrix} B'_x \\ B'_y \\ B'_z \\ E'_x \\ E'_y \\ E'_z \\ \chi^{-1}\phi' \\ (c'^2\beta)^{-1}\psi' \end{pmatrix} \qquad \mathbf{S} = -\Gamma \begin{pmatrix} 0 \\ 0 \\ 0 \\ J'_x \\ J'_y \\ J'_z \\ \chi'\rho' \\ 0 \end{pmatrix}$$

In VERTEX, Equation 21 is solved implicitly in time using the SUPG finite-element method [6]. The SUPG method utilizes the Galerkin form of Equation 21 and adds a stream-wise upwind stabilization term. After the application of Green's theorem it becomes [8]:

$$
\begin{aligned}
&\int\int\int_{\Omega}\Big[w+\big(\frac{\partial w}{\partial x}\mathbf{M}_x+\frac{\partial w}{\partial y}\mathbf{M}_y+\frac{\partial w}{\partial z}\mathbf{M}_z\big)\tau\Big]\Big[\frac{\partial \mathbf{U}}{\partial t}+\mathbf{S}\Big]\partial\Omega+\\
&\int\int_{\Xi}w\Big(\mathbf{F}_x\eta_x+\mathbf{G}_y\eta_y+\mathbf{H}_z\eta_z\Big)\partial\Xi-\int\int\int_{\Omega}\big(\frac{\partial w}{\partial x}\mathbf{F}_x+\frac{\partial w}{\partial y}\mathbf{G}_y+\frac{\partial w}{\partial z}\mathbf{H}_z\big)\partial\Omega\\
&\int\int\int_{\Omega}\Big[\big(\frac{\partial w}{\partial x}\mathbf{M}_x+\frac{\partial w}{\partial y}\mathbf{M}_y+\frac{\partial w}{\partial z}\mathbf{M}_z\big)\tau\Big]\Big[\frac{\partial \mathbf{F}_x}{\partial x}+\frac{\partial \mathbf{G}_y}{\partial y}+\frac{\partial \mathbf{H}_z}{\partial z}\Big]\partial\Omega=0
\end{aligned}
\tag{22}
$$

The SUPG method is differentiated from other methods with the use of the $(\frac{\partial w}{\partial x}\mathbf{M}_x+\frac{\partial w}{\partial y}\mathbf{M}_y+\frac{\partial w}{\partial z}\mathbf{M}_z)\tau$ stabilization term, where $\tau$ is the stabilization matrix (Section 2.4), and $w$ is a weighting function. For tetrahedrons, $w$ is determined from the shape function $N_i(\xi,\eta,\rho)$ and an arbitrary displacement $d_i$ [9]:

$$
w=\sum_{i=1}^{N_{nodes}}N_i(\xi,\eta,\rho)d_i \tag{23}
$$

The matrices $\mathbf{M}_x$, $\mathbf{M}_y$, and $\mathbf{M}_z$, are defined by the system of equations under consideration. For the Maxwell system (Equations 13–16):

$$
\mathbf{M}_x=\frac{\partial \mathbf{F}_x}{\partial \mathbf{U}}=\begin{pmatrix}
0 & 0 & 0 & 0 & 0 & 0 & 0 & c'^2\beta'^2\\
0 & 0 & 0 & 0 & 0 & -1 & 0 & 0\\
0 & 0 & 0 & 0 & 1 & 0 & 0 & 0\\
0 & 0 & 0 & 0 & 0 & 0 & c'^2\chi'^2 & 0\\
0 & 0 & c'^2 & 0 & 0 & 0 & 0 & 0\\
0 & -c'^2 & 0 & 0 & 0 & 0 & 0 & 0\\
0 & 0 & 0 & 1 & 0 & 0 & 0 & 0\\
1 & 0 & 0 & 0 & 0 & 0 & 0 & 0
\end{pmatrix} \tag{24}
$$

$$
\mathbf{M}_y=\frac{\partial \mathbf{G}_y}{\partial \mathbf{U}}=\begin{pmatrix}
0 & 0 & 0 & 0 & 0 & 1 & 0 & 0\\
0 & 0 & 0 & 0 & 0 & 0 & 0 & c'^2\beta'^2\\
0 & 0 & 0 & -1 & 0 & 0 & 0 & 0\\
0 & 0 & -c'^2 & 0 & 0 & 0 & 0 & 0\\
0 & 0 & 0 & 0 & 0 & 0 & c^2\chi'^2 & 0\\
c'^2 & 0 & 0 & 0 & 0 & 0 & 0 & 0\\
0 & 0 & 0 & 0 & 1 & 0 & 0 & 0\\
0 & 1 & 0 & 0 & 0 & 0 & 0 & 0
\end{pmatrix} \tag{25}
$$

$$
\mathbf{M}_z=\frac{\partial \mathbf{H}_z}{\partial \mathbf{U}}=\begin{pmatrix}
0 & 0 & 0 & 0 & -1 & 0 & 0 & 0\\
0 & 0 & 0 & 1 & 0 & 0 & 0 & 0\\
0 & 0 & 0 & 0 & 0 & 0 & 0 & c^2\beta'^2\\
0 & c'^2 & 0 & 0 & 0 & 0 & 0 & 0\\
-c'^2 & 0 & 0 & 0 & 0 & 0 & 0 & 0\\
0 & 0 & 0 & 0 & 0 & 0 & c'^2\chi'^2 & 0\\
0 & 0 & 0 & 0 & 0 & 1 & 0 & 0\\
0 & 0 & 1 & 0 & 0 & 0 & 0 & 0
\end{pmatrix} \tag{26}
$$

The eigenvalues for the matrices given by Equations 24–26 are $\pm c'$, $\pm \beta' c'$, and $\pm \chi' c'$, which represent the propagation of an electromagnetic wave and the $\phi'$ and $\psi'$ correction potential waves.

## 2.4 THE STABILIZATION MATRIX

The stabilization matrix $\tau$ is defined by the Gauss points within an element [8, 6]:

$$\tau = \Big( \sum_{i=1}^{N_{nodes}} |\frac{\partial N_i}{\partial x_j} \mathbf{M}_j| \Big)^{-1} \tag{27}$$

for $j = 1, 2, 3$. For a linear element the stabilization matrix ($N_{nodes} = 4$), $\tau$ becomes:

$$\begin{aligned} &\tau = \\ &\Big( \Big| \frac{\partial N_1}{\partial x} \mathbf{M}_x + \frac{\partial N_1}{\partial y} \mathbf{M}_y + \frac{\partial N_1}{\partial z} \mathbf{M}_z \Big| + \Big| \frac{\partial N_2}{\partial x} \mathbf{M}_x + \frac{\partial N_2}{\partial y} \mathbf{M}_y + \frac{\partial N_2}{\partial z} \mathbf{M}_z \Big| + \\ &\Big| \frac{\partial N_3}{\partial x} \mathbf{M}_x + \frac{\partial N_3}{\partial y} \mathbf{M}_y + \frac{\partial N_3}{\partial z} \mathbf{M}_z \Big| + \Big| \frac{\partial N_4}{\partial x} \mathbf{M}_x + \frac{\partial N_4}{\partial y} \mathbf{M}_y + \frac{\partial N_4}{\partial z} \mathbf{M}_z \Big| \Big)^{-1} \end{aligned} \tag{28}$$

Equation 28 contains several terms with the form $\left| N_x \mathbf{M}_x + N_y \mathbf{M}_y + N_z \mathbf{M}_z \right|$ where we have denoted $N_q = \partial_q(N_i)$ for each coordinate $q$. Utilizing this simplified notation, each term in the stabilization matrix takes the form:

$$\begin{aligned} &\left| N_x \mathbf{M}_x + N_y \mathbf{M}_y + N_z \mathbf{M}_z \right| = \\ &\begin{pmatrix} 0 & 0 & 0 & 0 & -N_z & N_y & 0 & c'^2 \beta'^2 N_x \\ 0 & 0 & 0 & N_z & 0 & -N_x & 0 & c'^2 \beta'^2 N_y \\ 0 & 0 & 0 & -N_y & N_x & 0 & 0 & c'^2 \beta'^2 N_z \\ 0 & c'^2 N_z & -c'^2 N_y & 0 & 0 & 0 & c'^2 \chi'^2 N_x & 0 \\ -c'^2 N_z & 0 & c'^2 N_x & 0 & 0 & 0 & c'^2 \chi'^2 N_y & 0 \\ c'^2 N_y & -c'^2 N_x & 0 & 0 & 0 & 0 & c'^2 \chi'^2 N_z & 0 \\ 0 & 0 & 0 & N_x & N_y & N_z & 0 & 0 \\ N_x & N_y & N_z & 0 & 0 & 0 & 0 & 0 \end{pmatrix} \end{aligned} \tag{29}$$

Equation 29 can also be written in diagonal form $\left| N_x \mathbf{M}_x + N_y \mathbf{M}_y + N_z \mathbf{M}_z \right| = \mathbf{T} \mathbf{\Lambda} \mathbf{T}^{-1}$, where $\mathbf{T}$ is the matrix of right eigenvectors, and $\mathbf{\Lambda}$ is the diagonal matrix of eigenvalues. For Equation 29:

$$\mathbf{T} = \begin{pmatrix} -\frac{N_y}{c'\mathscr{N}} & \frac{N_z}{c'\mathscr{N}} & \frac{N_y}{c'\mathscr{N}} & -\frac{N_z}{c'\mathscr{N}} & -\frac{c'\beta' N_x}{\mathscr{N}} & \frac{c'\beta' N_x}{\mathscr{N}} & 0 & 0 \\ \frac{N_x^2+N_z^2}{c\mathscr{N}N_x} & \frac{N_y N_z}{c\mathscr{N}N_x} & -\frac{N_x^2+N_z^2}{c'\mathscr{N}N_x} & -\frac{N_y N_z}{c'\mathscr{N}N_x} & -\frac{c'\beta' N_y}{\mathscr{N}} & \frac{c'\beta' N_y}{\mathscr{N}} & 0 & 0 \\ -\frac{N_y N_z}{c'\mathscr{N}N_x} & -\frac{N_x^2+N_y^2}{c'\mathscr{N}N_x} & \frac{N_y N_z}{c'\mathscr{N}N_x} & \frac{N_x^2+N_y^2}{c'\mathscr{N}N_x} & -\frac{c'\beta' N_z}{\mathscr{N}} & \frac{c'\beta' N_z}{\mathscr{N}} & 0 & 0 \\ -\frac{N_z}{N_x} & -\frac{N_y}{N_x} & -\frac{N_z}{N_x} & -\frac{N_y}{N_x} & 0 & 0 & -\frac{c'\chi' N_x}{\mathscr{N}} & \frac{c'\chi' N_x}{\mathscr{N}} \\ 0 & 1 & 0 & 1 & 0 & 0 & -\frac{c'\chi' N_y}{\mathscr{N}} & \frac{c'\chi' N_y}{\mathscr{N}} \\ 1 & 0 & 1 & 0 & 0 & 0 & -\frac{c''\chi' N_z}{\mathscr{N}} & \frac{c'\chi' N_z}{\mathscr{N}} \\ 0 & 0 & 0 & 0 & 0 & 0 & 1 & 1 \\ 0 & 0 & 0 & 0 & 1 & 1 & 0 & 0 \end{pmatrix} \tag{30}$$

$$\mathbf{\Lambda} = \begin{pmatrix} -c'\mathscr{N} & 0 & 0 & 0 & 0 & 0 & 0 & 0 \\ 0 & -c'\mathscr{N} & 0 & 0 & 0 & 0 & 0 & 0 \\ 0 & 0 & c'\mathscr{N} & 0 & 0 & 0 & 0 & 0 \\ 0 & 0 & 0 & c'\mathscr{N} & 0 & 0 & 0 & 0 \\ 0 & 0 & 0 & 0 & -c'\beta'\mathscr{N} & 0 & 0 & 0 \\ 0 & 0 & 0 & 0 & 0 & \beta' c'\mathscr{N} & 0 & 0 \\ 0 & 0 & 0 & 0 & 0 & 0 & -c'\chi'\mathscr{N} & 0 \\ 0 & 0 & 0 & 0 & 0 & 0 & 0 & c'\chi'\mathscr{N} \end{pmatrix} \tag{31}$$

$$\mathbf{T}^{-1} = \begin{pmatrix} -\frac{c' N_y}{2\mathscr{N}} & \frac{c' N_x}{2\mathscr{N}} & 0 & -\frac{N_x N_z}{2n^2} & -\frac{N_y N_z}{2n^2} & \frac{N_x^2+N_y^2}{2n^2} & 0 & 0 \\ \frac{c' N_z}{2\mathscr{N}} & 0 & -\frac{c' N_x}{2\mathscr{N}} & -\frac{N_x N_y}{2n^2} & \frac{N_x^2+N_z^2}{2n^2} & -\frac{N_y N_z}{2n^2} & 0 & 0 \\ \frac{c' N_y}{2\mathscr{N}} & -\frac{c' N_x}{2\mathscr{N}} & 0 & -\frac{N_x N_z}{2n^2} & -\frac{N_y N_z}{2n^2} & \frac{N_x^2+N_y^2}{2n^2} & 0 & 0 \\ -\frac{c' N_z}{2\mathscr{N}} & 0 & \frac{c' N_x}{2\mathscr{N}} & -\frac{N_x N_y}{2n^2} & \frac{N_x^2+N_z^2}{2n^2} & -\frac{N_y N_z}{2n^2} & 0 & 0 \\ -\frac{N_x}{2c'\beta'\mathscr{N}} & -\frac{N_y}{2c'\beta'\mathscr{N}} & -\frac{N_z}{2c'\beta'\mathscr{N}} & 0 & 0 & 0 & 0 & \frac{1}{2} \\ \frac{N_x}{2c'\beta'\mathscr{N}} & \frac{N_y}{2c'\beta'\mathscr{N}} & \frac{N_z}{2c'\beta'\mathscr{N}} & 0 & 0 & 0 & 0 & \frac{1}{2} \\ 0 & 0 & 0 & -\frac{N_x}{2c'\chi'\mathscr{N}} & -\frac{N_y}{2c'\chi'\mathscr{N}} & -\frac{N_z}{2c'\chi'\mathscr{N}} & \frac{1}{2} & 0 \\ 0 & 0 & 0 & \frac{N_x}{2c'\chi'\mathscr{N}} & \frac{N_y}{2c'\chi'\mathscr{N}} & \frac{N_z}{2c'\chi'\mathscr{N}} & \frac{1}{2} & 0 \end{pmatrix} \tag{32}$$

where $\mathscr{N} = \sqrt{N_x^2 + N_y^2 + N_z^2}$. Using the matrices given in Equations 30–32:

$$\mathbf{T}|\mathbf{\Lambda}|\mathbf{T}^{-1} = \begin{bmatrix} \frac{c'\left(\beta' N_x^2+N_y^2+N_z^2\right)}{\mathscr{N}} & \frac{(\beta'-1)c' N_x N_y}{\mathscr{N}} & \frac{(\beta'-1)c' N_x N_z}{\mathscr{N}} & 0 \\ \frac{(\beta'-1)c' N_x N_y}{\mathscr{N}} & \frac{c'\left(N_x^2+\beta' N_y^2+N_z^2\right)}{\mathscr{N}} & \frac{(\beta'-1)c' N_y N_z}{\mathscr{N}} & 0 \\ \frac{(\beta'-1)c' N_x N_z}{\mathscr{N}} & \frac{(\beta'-1)c' N_y N_z}{\mathscr{N}} & \frac{c'\left(N_x^2+N_y^2+\beta' N_z^2\right)}{\mathscr{N}} & 0 \\ 0 & 0 & 0 & \frac{c'\left(N_x^2\chi'+N_y^2+N_z^2\right)}{\mathscr{N}} \\ 0 & 0 & 0 & \frac{c' N_x N_y(\chi'-1)}{\mathscr{N}} \\ 0 & 0 & 0 & \frac{c' N_x N_z(\chi'-1)}{\mathscr{N}} \\ 0 & 0 & 0 & 0 \\ 0 & 0 & 0 & 0 \end{bmatrix} \tag{33}$$

$$\begin{bmatrix} 0 & 0 & 0 & 0 \\ 0 & 0 & 0 & 0 \\ 0 & 0 & 0 & 0 \\ \frac{c' N_x N_y(\chi'-1)}{\mathscr{N}} & \frac{c' N_x N_z(\chi'-1)}{\mathscr{N}} & 0 & 0 \\ \frac{c'\left(N_x^2+N_y^2\chi'+N_z^2\right)}{\mathscr{N}} & \frac{c' N_y N_z(\chi'-1)}{\mathscr{N}} & 0 & 0 \\ \frac{c N_y N_z(\chi'-1)}{\mathscr{N}} & \frac{c'\left(N_x^2+N_y^2+N_z^2\chi'\right)}{\mathscr{N}} & 0 & 0 \\ 0 & 0 & c'\chi'\mathscr{N} & 0 \\ 0 & 0 & 0 & \beta' c'\mathscr{N} \end{bmatrix}$$

If $\chi' = 1$ and $\beta' = 1$, then Equation 33 is fully diagonalized:

$$\mathbf{T}|\mathbf{\Lambda}|\mathbf{T}^{-1} = c'\mathscr{N}\mathbf{I} = \begin{pmatrix} c'\mathscr{N} & 0 & 0 & 0 & 0 & 0 & 0 & 0 \\ 0 & c'\mathscr{N} & 0 & 0 & 0 & 0 & 0 & 0 \\ 0 & 0 & c'\mathscr{N} & 0 & 0 & 0 & 0 & 0 \\ 0 & 0 & 0 & c'\mathscr{N} & 0 & 0 & 0 & 0 \\ 0 & 0 & 0 & 0 & c'\mathscr{N} & 0 & 0 & 0 \\ 0 & 0 & 0 & 0 & 0 & c'\mathscr{N} & 0 & 0 \\ 0 & 0 & 0 & 0 & 0 & 0 & c'\mathscr{N} & 0 \\ 0 & 0 & 0 & 0 & 0 & 0 & 0 & c'\mathscr{N} \end{pmatrix} \tag{34}$$

where $\mathbf{I}$ is the identity matrix.

## 3. TEST PROBLEMS

Solutions obtained using VERTEX will be validated against several test cases. In Section 3.1, several cases in magnetostatics will be discussed. In Section 3.2, cases designed to test the ability to enforce the $\nabla \cdot \mathbf{E}$ and $\nabla \cdot \mathbf{B}$ constraints will be discussed. Finally, in Section 3.3, several full-wave cases will be examined.

## 3.1 TEST CASES IN MAGNETOSTATICS

In magnetostatic problems, we consider steady-state current density distributions ($\mathbf{J} = \mathbf{J}(x, y, z)$) with $\rho_q = 0$. The magnetic field in these situations is readily determined from the Biot-Savart law:

$$d\mathbf{B} = \mu_0 I \frac{d\mathbf{L} \times \mathbf{r'}}{4\pi|\mathbf{r'}|^3} \tag{35}$$

where $Id\mathbf{L}$ is the current element, and $\mathbf{r'}$ is the position vector. We now consider the solution to the Biot-Savart equation for specific cases of $\mathbf{J}(x, y, z)$.

### 3.1.1 Steady Current in an infinitely long wire

The magnetic field produced by an infinitely long current conducting wire is a common textbook problem useful for verification purposes. In this case $\mathbf{J} = J_0\delta(r)\hat{\mathbf{z}}$, and the application of the Biot-Savart provides the magnetic field outside the wire :

$$B_\theta = \frac{\mu_0 I}{2\pi r} \tag{36}$$

By utilizing the magnetic field profile predicted by Equation 36, test cases will be constricted in one, two, and three dimensions utilizing one or more wires placed in the computational domain. Figure 1 shows the field created with a single wire in one dimension, and two wires in three dimensions.

### 3.1.2 Steady Current in a loop

Consider the case of a loop of radius $R$ in the $x$-$y$ plane. In this case, $\mathbf{J} = J_0\delta(r - R)\delta(\theta - \pi/2)\hat{\theta}$, where $\theta$ is the polar angle. The application of the Biot-Savart law yields [10]:

$$\mathbf{B}_r = \frac{\mu_o I}{2R}\frac{1}{\pi\sqrt{Q}}\Big(E(k^2)\frac{1-\alpha^2-\beta^2}{Q-4R} + K(k^2)\Big). \tag{37}$$

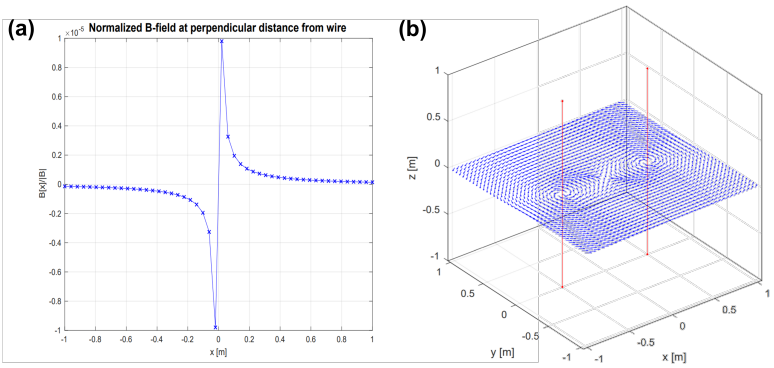


**Figure 1. Magnetic field profile of (a) a single wire with current aligned along the z-axis and (b) for two wires shown in red.**

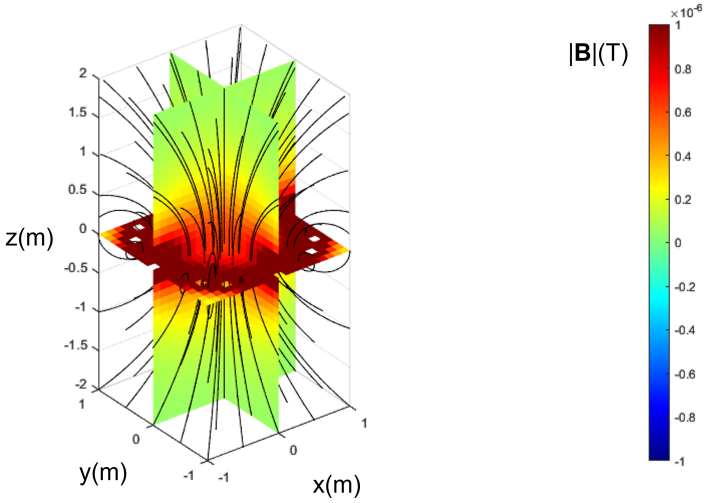


**Figure 2. Slice plot of |B| with steam lines for a current loop with $I$=1 A and $R$ = 1 m.**

$$\mathbf{B}_z = \frac{\mu_o I}{2R}\frac{\gamma}{\pi\sqrt{Q}}\Big(E(k^2)\frac{1+\alpha^2+\beta^2}{Q-4R} - K(k^2)\Big) \tag{38}$$

$$\alpha = r/R \tag{39}$$

$$\beta = z/R \tag{40}$$

$$\gamma = x/r \tag{41}$$

$$Q = (1+\alpha^2)+\beta^2 \tag{42}$$

$$k = \sqrt{(\frac{4\alpha}{Q}} \tag{43}$$

where the complete elliptic integral function is denoted as $K(k)$ for the first kind and as $E(k)$ for the second kind. The case of a current loop yields a magnetic field with a complex topology (Figure 2) sufficient for testing the Maxwell solver in VERTEX for 2D polar and 3D Cartesian geometries.

### 3.1.3 Steady Current in a solenoid

The magnetic field created from a steady current traveling through a tightly-packed solenoid is another good test case for the Maxwell solver. Solutions for a solenoid can be obtained directly from Equations 37–38 by superimposing many current loops. Figure 3 shows an example of the magnetic field distribution for a case of 50 identical current loops oriented parallel to the $x$-$y$ plane and uniformity separated in the axial direction.

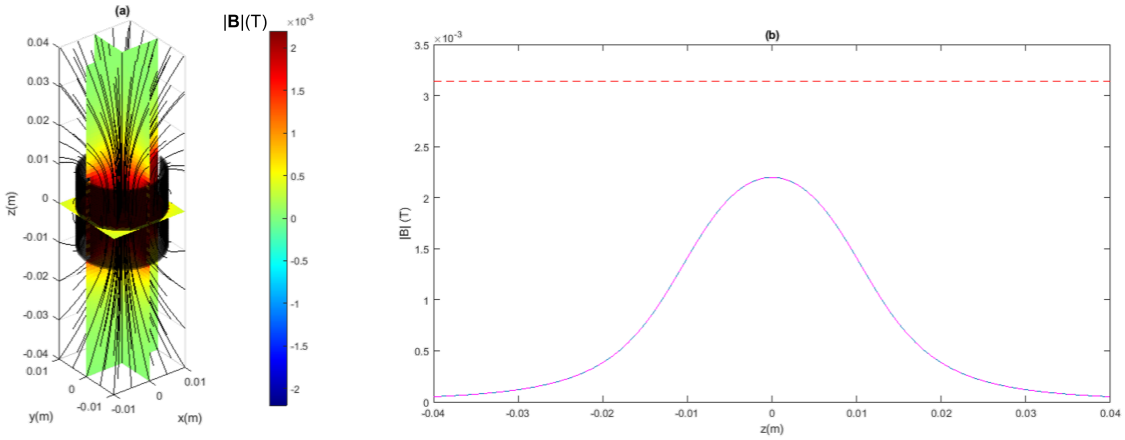


**Figure 3. (a) Magnetic field strength for 50 closely packed 1 cm radius loops carrying a current of 1 A ($L/R = 2$), where $L$ is the total length of the solenoid. (b) $B_z$ along the axis for the same case. The dotted red line shows the long solenoid limit ($L/R >> 1$), or where $B_z = \mu_0 In$ when $n$ is the number of turns per length.**

### 3.2 TEST CASES FOR DIVERGENCE CONSTRAINTS

The correction potentials introduced into Equations 13–16 provide a means to solve the system even in the case where the continuity equation (Equation 7) is not strictly valid:

$$\frac{\partial \rho_q}{\partial t} + \boldsymbol{\nabla} \cdot \mathbf{J} = \delta \tag{44}$$

where the right-hand side contains nonzero term $\delta$, which may characterize a physical source term (e.g., ionization, sputtering) or a non-physical numerical error that can quickly drive a solution to be unstable.

To test the ability of the correction potentials to enforce the divergence constraints in the Maxwell system, a test problem to consider is the case of a time-varying charge density located at the origin [4]:

$$\mathbf{J} = 0 \tag{45}$$

$$\rho_q = e sin(\omega t)\delta(\mathbf{r}) \tag{46}$$

where $\omega$ is an angular frequency. The conditions set by Equations 45–46 violate the continuity equation, but are still coupled into Equations 13–16 through the correction potential $\phi'$. This distribution gives rise to fields produced by a point charge located at the origin, and the analytical solution can be obtained using the retarded-time form of the scalar potential [10]:

$$\Phi(\mathbf{x}) = \frac{1}{4\pi\epsilon_0} \int \rho(\mathbf{x}') \frac{e^{ik|\mathbf{x}-\mathbf{x}'|}}{|\mathbf{x}-\mathbf{x}'|} d^3x' \tag{47}$$

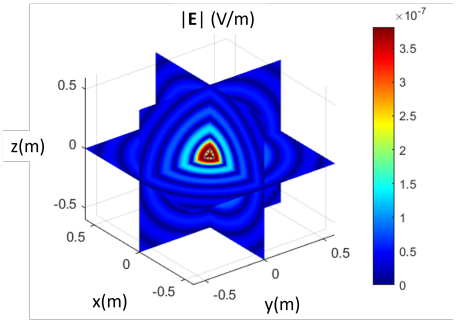


**Figure 4. |E| for the distribution given in Equations 45–46 with frequency of 1 Ghz.**

where **x** is the position vector and **x'** is the position vector integrated over the charge distribution $\rho$. Using Equations 45–46, integration yields

$$\Phi = \frac{\rho_0}{4\pi\epsilon_0} \frac{e^{ik\sqrt{x^2+y^2+z^2}}}{\sqrt{x^2+y^2+z^2}} \tag{48}$$

where the electric fields are simply $\mathbf{E} = -\nabla\Phi$. In figure 4 the electric field produced by an oscillating charge at a frequency of 1GHz is shown, where the amplitude is equal to an elementary charge unit $e$.

## 3.3 TEST CASES IN ELECTROMAGNETICS

### 3.3.1 Test Case: Time-varying Loop Antenna

A loop antenna [5] is typically constructed by passing a time-varying sinusoidal with angular frequency $\omega$ into a circular conductor of radius $a$. The electromagnetic fields radiated in this situation are characteristics based on the value of $a/\lambda$, where $\lambda$ is the wavelength.

For an electrically short antenna, the radiated fields can be determined analytically by computing the vector potential **A**. For an electrically short antenna, the current is assumed not to vary along the circumference of the antenna, which is typically physically valid if either (1) the loop is sufficiently small ($a/\lambda$ <<1) or (2) the loop is divided into several sections that are fed with phase-shifted sources to artificially force a constant current. In this case, $\mathbf{J} = J_0 sin(\omega t)\delta(r-R)\delta(\theta-\pi/2)\hat{\phi}$, and the vector potential only has components along the azimuthal direction $\hat{\phi}$. Integrating over the current distribution $\phi'$, $\mathbf{A} = A_\phi\hat{\phi}$ and:

$$A_\phi = \frac{\mu_0 J_0}{4\pi}\int_0^{2\pi} \frac{e^{ik(a^2+r^2-2arsin(\theta)cos(\phi'))^{1/2}}}{(a^2+r^2-2arsin(\theta)cos(\phi'))^{1/2}} cos(\phi')d\phi' \tag{49}$$

Once **A** is known, the magnetic field and electric field [10] can be computed from $\mathbf{B} = \nabla \times \mathbf{A}$ and $\mathbf{E} = ic\nabla \times \mathbf{B}$. Equation 49 is valid provided that the current is kept constant along the circumference of the loop, and can be solved numerically to obtain the electric and magnetic fields for any value of $a/\lambda$ (Figure 5).

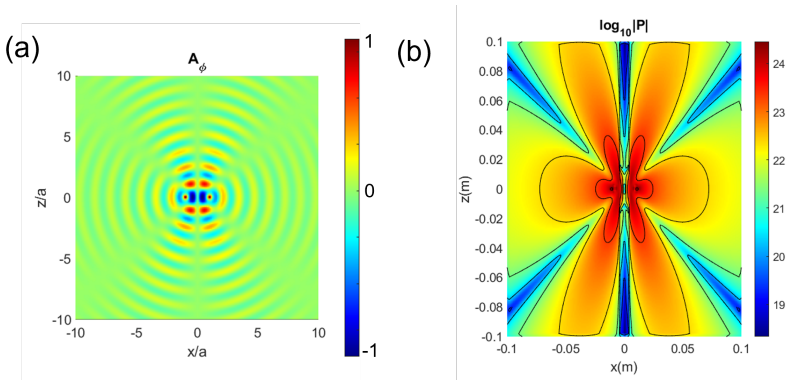


**Figure 5. (a) $A_\phi$ (in arbitray units) for $a/\lambda$=0.8, and (b) the log of the radiated power, defined by $|\mathbf{P}| = 1/(2\mu_0)\mathbf{E} \times \mathbf{B}^*$ when $a$=1 cm, $I$=1A, and f = 23.9 Ghz. The characteristic lobed structure for a loop antenna is clearly visable.**

### 3.3.2 Mie Scattering

The properties of a plane wave scattered from a sphere located at the origin were first considered for the case of a perfectly conducting sphere by Mie, and was later expanded to pure and radially varying dielectric distributions. For the purposes of this work, Mie solutions will be leveraged to provide a validation for VERTEX-MAXWELL.

Mie solutions are derived by considering the case where an incident electromagnetic wave propagating in the -$\hat{\mathbf{z}}$ direction encounters a sphere located at the origin. The incident fields are

$$\mathbf{E}^i = E_0 e^{-ik_0 z}\hat{\mathbf{x}} \tag{50}$$

$$\mathbf{H}^i = -E_0/\eta e^{-ik_0 z}\hat{\mathbf{y}} \tag{51}$$

The generalized Mie solution for the scattered fields takes the form [1]:

$$\mathbf{E}^s(r',\theta',\phi',\omega) = E_0 \sum_{n=1}^{\infty}\left(A_n\mathbf{M}_{o,1,n} + B_n\mathbf{N}_{e,1,n}\right) \tag{52}$$

$$\mathbf{H}^s(r',\theta',\phi',\omega) = -i\sqrt{\frac{\epsilon_0}{\mu_0}}E_0 \sum_{n=1}^{\infty}\left(A_n\mathbf{M}_{e,1,n} + B_n\mathbf{N}_{o,1,n}\right) \tag{53}$$

at the observation point $(r',\theta',\phi')$, where $A_n$ and $B_n$ are coefficients that depend on the specific properties of the sphere, which will be considered later. The vector quantities are defined by

$$\mathbf{M}_{e,1,n} = \begin{pmatrix} 0\hat{r} \\ -\frac{1}{sin(\theta)}h^{(1)}(k_o r')P_n^1(cos(\theta'))sin(\phi')\hat{\theta} \\ -h^{(1)}(k_o r')\frac{d}{d\theta}P_n^1(cos(\theta'))cos(\phi')\hat{\phi} \end{pmatrix} \tag{54}$$

$$\mathbf{M}_{o,1,n} = \begin{pmatrix} 0\hat{r} \\ \frac{1}{sin(\theta)} h^{(1)}(k_o r') P_n^1(cos(\theta')) cos(\phi')\hat{\theta} \\ -h^{(1)}(k_o r') \frac{d}{d\theta} P_n^1(cos(\theta')) sin(\phi')\hat{\phi} \end{pmatrix} \tag{55}$$

$$\mathbf{N}_{e,1,n} = \begin{pmatrix} \frac{n(n+1)}{k_o r'} h^{(1)}(k_o r') P_n^1(cos(\theta')) cos(\phi')\hat{r} \\ \frac{1}{k_o r'} \frac{d}{d(k_o r')}(k_o r' h^{(1)}(k_o r')) \frac{d}{d\theta}(P_n^1(cos(\theta'))) cos(\phi')\hat{\theta} \\ -\frac{1}{k_o r' sin(\theta')} \frac{d}{d(k_o r')}(k_o r' h^{(1)}(k_o r')) P_n^1(cos(\theta')) sin(\phi')\hat{\phi} \end{pmatrix} \tag{56}$$

$$\mathbf{N}_{o,1,n} = \begin{pmatrix} \frac{n(n+1)}{k_o r'} h^{(1)}(k_o r') P_n^1(cos(\theta')) sin(\phi')\hat{r} \\ \frac{1}{k_o r'} \frac{d}{d(k_o r')}(k_o r' h^{(1)}(k_o r')) \frac{d}{d\theta}(P_n^1(cos(\theta'))) sin(\phi')\hat{\theta} \\ \frac{1}{k_o r' sin(\theta')} \frac{d}{d(k_o r')}(k_o r' h^{(1)}(k_o r')) P_n^1(cos(\theta')) cos(\phi')\hat{\phi} \end{pmatrix} \tag{57}$$

where $h^{(1)}$ are spherical Hankel functions and $P_n^1$ are the associated Legendre functions. Equations 52–57 are valid for any value of $k_0 r'$, and thus can be used to compute the near ($r' << a$) and far ($r' >> a$) scattered fields. With information of the scattered fields, it is possible to compute the scattering cross section of a sphere, which are defined as

$$\sigma = 4\pi \lim_{r->\infty} \left( \frac{\mathbf{E} \cdot \mathbf{E^*}}{E_0} \right) \tag{58}$$

where **E*** is the complex conjugate of the vector **E**.

**Perfectly Conducting Spheres** The coefficients $A_n$ and $B_n$ are defined based on the properties of the sphere. For a perfectly conducting sphere, these coefficients become [1]

$$A_n = -(-i)^n \frac{2n+1}{n(n+1)} \frac{j_n(k_o a)}{h^{(1)}(k_o a)} \tag{59}$$

$$B_n = (-i)^{n+1} \frac{2n+1}{n(n+1)} \frac{[k_o a j_n(k_o a)]'}{[k_o a h^{(1)}(k_o a)]'} \tag{60}$$

where $j_n$ is a spherical Bessel function for the first kind, and the prime denotes differentiation of the functions contained within the brackets with respect to $k_0 a$. With the generalized solutions Equations 52–53, along with Equations 59–60 and Equations 54–57, the scattered field can be obtained using a tool such as MATLAB or Wolfram Mathematica. An example of the solved equations, obtained in MATLAB, is shown in Figure 6.

In VERTEX, the fields scattered from a perfectly conducting sphere can be attained by injecting the incident wave from the boundaries, and using a conductive boundary condition in the interior of the computational domain to treat the sphere. In the free space region of the domain, $\mathbf{J} = 0$ and $\rho_q = 0$.

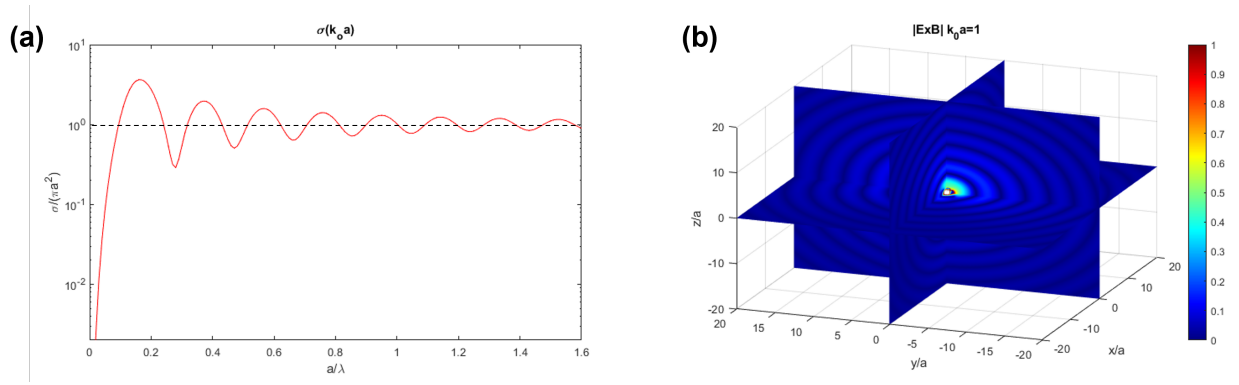


**Figure 6. (a) Plot of the normalized backscatter cross section (for $\theta = 0$ and $\phi = 0$) as a function of $a/\lambda$. The plot shows the Rayleigh region for $a/\lambda < 0.2$, and the tendency for $\sigma \to \pi a^2$ for large values of $a/\lambda$. (b) The normalized scattered power for $k_0 a = 1$**

**Dielectric Spheres** For dielectric spheres with a propagation wave vector of $k_1$, the forms of $A_n$ and $B_n$ are [1]:

$$A_n = (-i)^n \frac{2n+1}{n(n+1)} \Big[ \frac{j_n(k_o a)[k_1 a j_n(k_1 a)]' - j_n(k_1 a)[k_o a j_n(k_o a)]'}{j_n(k_1 a)[k_0 a h_n^{(1)}(k_o a)]' - h^{(1)}(k_o a)[k_1 a j_n(k_1 a)]'} \Big] \tag{61}$$

$$B_n = (-i)^{n+1} \frac{2n+1}{n(n+1)} \Big[ \frac{j_n(k_o a)[k_1 a j_n(k_1 a)]' - m_1^2 j_n(k_1 a)[k_o a j_n(k_o a)]'}{h_n^{(1)}(k_o a)[k_1 a j_n(k_1 a)]' - m_1^2 j(k_1 a)[k_o a h_n^{(1)}(k_o a)]'} \Big] \tag{62}$$

where the prime denotes differentiation $k_0 a$ or $k_1 a$ and $k_1 = k_0 m_1$.

**Radially layered spheres** The scattered fields can also be computed exactly for spheres composed of layers that are homogeneous in the azimuthal and polar directions, which vary radially. An exact solution has been derived in this case [1], by considering $N$ spherical layers, each of thickness $\tau_l$, and with electromagnetic properties $\epsilon_l$ and $\mu_l$ (where $l = 0, 1, ...N$). In the cited work, the exact expressions are readily solved by computing the effective values for $A_n$ and $B_n$ using a MATLAB script.

One specific case to consider is the case of an exponential distribution for the radial profile:

$$\epsilon_r(r) = 1 - (\omega_p/\omega)^2 \frac{e^{-r/a}}{1 - i\nu/\omega} \tag{63}$$

where $\omega_p$ is the plasma frequency, $\omega$ is the incident wave frequency, and $\nu$ characterizes collisions. The value of $\epsilon$ is entirely governed by the ratios $\omega_p/\omega$ and $\nu/\omega$. For example, when $\omega_p/\omega > 1$, $\epsilon$ tends to negative values representing metallic behavior at smaller radii.

Using the exponential distribution, the radar cross section can be determined by using the scattered fields determined from the Mie solutions for a sphere with a sufficient number of layers to resolve the distribution. In Figure 7, the backscatter cross section is shown computed with a MATLAB script for several values. The results compare agreeably to results in open literature [11] (see Figure 1 provided in the reference).

The team will compare predictions made by VERTEX-MAXWELL with those obtained using Mie solutions for radially inhomogenous spheres. The distributions tested will be chosen from literature

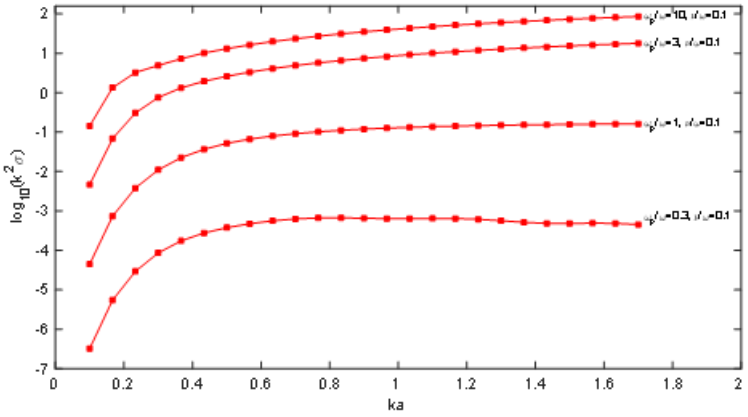


**Figure 7. Radar backscatter as a function of $ka$ for various values of $\omega_p/\omega$ and $\nu/\omega$, for the distribution given in Equation 63. The layered-sphere Mie solution derived by Ruck [1] was utilized, along with 200 individual spherical layers to capture the distribution.**

[11, 12], and provide a means to test the solver when strong spatial gradients are present in $\epsilon_r$. The team will also test the ability of the solver to function in the numerically unfavorable limit where $\epsilon_r$ takes a negative value and therefore acts as a conductor.

# 4. WORK PLAN

## 4.1 MILESTONES

The project has the following Milestones:

- **Milestone 1 (12/31/22):** Derivation of eigensystem for fully coupled Maxwell's equations, including the correction potentials (or Lagrange multipliers).
- **Milestone 2 (6/30/23):** Implementation of Maxwell's equations in two spatial dimensions (cartesian and polar) in the VERTEX-CORE framework with up-winding enabled.
- **Milestone 3 (12/31/23)**: Implementation of Maxwell's equations in three spatial dimensions in the VERTEX-CORE framework with up-winding enabled.
- **Milestone 4 (9/30/23)**: Implementation of boundary condition field closure terms consistent with the volumetric finite-element terms. Material interfaces will be represented by numerical jumps in current, permeability, or permittivity.
- **Milestone 5 (9/30/25)**: Verify numerical order of accuracy for electromagnetic field for the cases, described in Section 3., and experimentally obtained data. L1 and L2 error norms will be plotted to ensure the anticipated numerical order of accuracy from the finite-element discretization method is achieved.

## References


[1] George Ruck. *Radar Cross Section Handbook: Volume 1 Volume 1 of Radar Cross Section Handbook*. Bantam, Springer US, 1970.

[2] Franklin Curtis. Vertex advanced multiphysics simulations for core applications. *ORNL LDRD proposal*, 2023.

[3] Roscoe A Bartlett, David M Gay, and Eric T Phipps. Automatic differentiation of c++ codes for large-scale scientific computing. In *Computational Science–ICCS 2006: 6th International Conference, Reading, UK, May 28-31, 2006, Proceedings, Part IV 6*, pages 525–532. Springer, 2006.

[4] Claus-Dieter Munz, Rudolf Schneider, and Ursula Voß. A finite-volume method for the maxwell equations in the time domain. *SIAM Journal on Scientific Computing*, 22(2):449–475, 2000.

[5] Constantine A Balanis. *Advanced engineering electromagnetics*. John Wiley & Sons, 2012.

[6] Thomas JR Hughes and Michel Mallet. A new finite element formulation for computational fluid dynamics: Iii. the generalized streamline operator for multidimensional advective-diffusive systems. *Computer methods in applied mechanics and engineering*, 58(3):305–328, 1986.

[7] Youcef Saad and Martin H Schultz. Gmres: A generalized minimal residual algorithm for solving nonsymmetric linear systems. *SIAM Journal on scientific and statistical computing*, 7(3):856–869, 1986.

[8] Ryan Steven Glasby. *Computational design for electromagnetic simulations*. PhD thesis, The University of Tennessee at Chattanooga, 2011.

[9] Thomas JR Hughes. *The finite element method: linear static and dynamic finite element analysis*. Courier Corporation, 2012.

[10] John David Jackson. Classical electrodynamics, 1999.

[11] P Bisbing. Electromagnetic scattering by an exponentially inhomogeneous plasma sphere. *IEEE Transactions on Antennas and Propagation*, 14(2):219–224, 1966.

[12] J Mikulski and E Murphy. The computation of electromagnetic scattering from concentric spherical structures. *IEEE Transactions on Antennas and Propagation*, 11(2):169–177, 1963.